Received: Added at production | Revised: Added at production | Accepted: Added at production

DOI: xxx/xxxx

RESEARCH ARTICLE

DF-QSM: Data Fidelity based Hybrid Approach for Improved Quantitative Susceptibility Mapping of the Brain

Naveen Paluru[1] | Raji Susan Mathew[2] | Phaneendra K. Yalavarthy*[1]

[1]Department of Computational and Data Sciences, Indian Institute of Science, Bangalore, Karnataka, India
[2]School of Data Science, Indian Institute of Science Education and Research, Thiruvananthapuram, Kerala, India

Correspondence
*Phaneendra K. Yalavarthy. Email: yalavarthy@iisc.ac.in

Abstract

Quantitative Susceptibility Mapping (QSM) is an advanced magnetic resonance imaging (MRI) technique to quantify the magnetic susceptibility of the tissue under investigation. Deep learning methods have shown promising results in deconvolving the susceptibility distribution from the measured local field obtained from the MR phase. Although existing deep learning based QSM methods can produce high-quality reconstruction, they are highly biased toward training data distribution with less scope for generalizability. This work proposes a hybrid two-step reconstruction approach to improve deep learning based QSM reconstruction. The susceptibility map prediction obtained from the deep learning methods has been refined in the framework developed in this work to ensure consistency with the measured local field. The developed method was validated on existing deep learning and model-based deep learning methods for susceptibility mapping of the brain. The developed method resulted in improved reconstruction for MRI volumes obtained with different acquisition settings, including deep learning models trained on constrained (limited) data settings.

KEYWORDS:
dipole deconvolution, deep learning, generalizability, reconstruction, susceptibility map

1 | INTRODUCTION

Quantitative susceptibility mapping (QSM) is a magnetic resonance (MR) based parametric imaging method measuring tissue magnetic susceptibility. Key applications of QSM include the assessment of various brain disorders, such as brain hemorrhage, multiple sclerosis, and Parkinson's disease[1]. The QSM method has been used to estimate myelin and iron concentrations in the brain[2,3,4]. Similarly, the other immediate application of QSM includes differentiating calcification from blood deposits[5]. The susceptibility maps are generated by using the measured magnetic field distribution (effect) to derive the local tissue magnetic susceptibility (source). Simply, QSM involves deconvolving the susceptibility distribution from the relative difference field (also known as the local field or tissue phase) obtained from the phase information of the MR image. The relationship between the local field $\mathrm{y}(r)$ and the susceptibility $\mathrm{x}(r)$ is as shown below:

$$\mathrm{y}(r) = \frac{1}{4\pi} \int_{r' \neq r}^{R^3} \mathrm{x}(r') \frac{3\cos^2\Theta - 1}{|r - r'|^3} dr', \tag{1}$$

where, r is a spatial location [x,y,z] in the three-dimensional (3D) MR volume, Θ is the angle between the unit vector along $r - r'$ and the unit vector along the direction of the main magnetic field during MR acquisition. The relation in Eq. (1) can be written as a convolution operation ($\otimes$)

[0]**Abbreviations:** QSM, quantitative susceptibility mapping; SSIM, structural similarity index measure; PSNR, peak signal-to-noise ratio; NMSE, normalized mean squared error; HFEN, high-frequency error norm

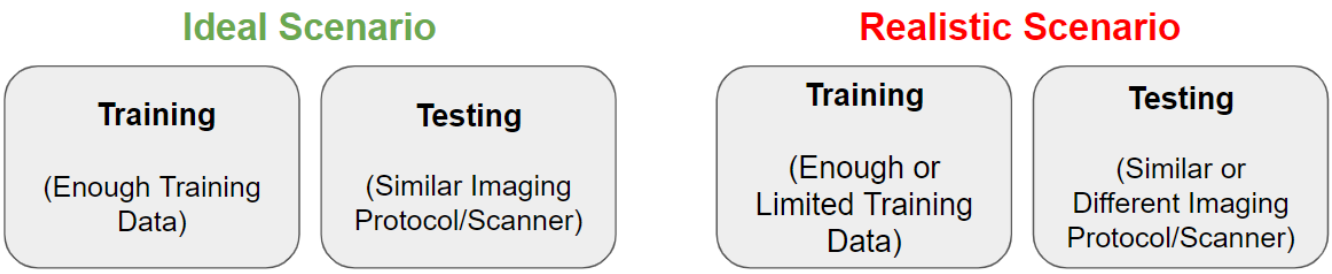

Figure 1 An overview of different experimental conditions expected in the context of automated deep learning based medical image analysis.

between $x(r)$ and $d(r)$ (dipole kernel) as shown in Eq. (2). Given the dipole kernel $d(r)$ (shown in Eq. (3)) and the measured local field $y(r)$, Eq. (2) needs to be deconvolved to reconstruct susceptibility $x(r)$. In the Fourier domain, Eq. (2) can also be represented in matrix form as shown in Eq. (4), where $\phi = F^H D F$, F is the matrix representation of the Fourier transform and D is the diagonal matrix with entries equal to the Fourier coefficients of the dipole kernel. As the dipole kernel has zeros on the conical surface, the frequency content of x is undersampled, and hence solving for x leads to an ill-posed problem. The ill-posedness of the QSM reconstruction problem can be mitigated by using multiple orientation sampling that leads to well-conditioned inversion as in the case of calculation of susceptibility through multiple orientation sampling (COSMOS)[6] (a reliable method for estimating QSM, taking into account the isotropic magnetic susceptibility of the source in any B_0 field orientation). As this requires data from multiple orientations, the data acquisition time is prohibitively long, leading to patient discomfort. Therefore, single-orientation-based QSM reconstruction methods have been proposed in the literature, ranging from conventional closed-form, iterative, deep learning, and model-based deep learning methods.

$$y(r) = x(r) \otimes d(r) \tag{2}$$

$$d(r) = \frac{3\cos^2\Theta - 1}{4\pi|r|^3} \tag{3}$$

$$\phi x = y \tag{4}$$

Conventional techniques such as TKD[7], L2[8], and SDI[9] have proposed closed-form solutions by truncating the dipole kernel[7], regularizing the pseudo-inverse[8], and correction of inversion artifacts[9] for the reconstruction of the susceptibility map from the measured local field. These methods have been the most efficient in terms of reconstruction time and computational expense. However, due to the ill-posedness of the QSM problem, such closed-form methods suffer from streaking artifacts. On the other hand, iterative methods such as morphology-enabled dipole inversion (MEDI)[10,11], non-linear dipole inversion (NDI)[12] and hybrid data fidelity QSM (HD-QSM, also referred as L1L2)[13] have improved susceptibility reconstruction compared to closed form methods. Specifically, MEDI incorporates structural consistency of the magnitude images as a regularized constraint to improve the quality of susceptibility maps. NDI demonstrated that a high-quality QSM can be iteratively generated using non-linear data fidelity without explicit regularization. The HD-QSM approach involves a two-step process, where it initially seeks a solution for the L1-norm based linear data consistency and subsequently employs this solution as an initialization for the L2-norm based linear data consistency. A TV regularizer has been used for the L1 and L2 steps of HD-QSM. This hybrid approach showed that using a previous reconstruction as an initial point for the reconstruction of susceptibility maps is robust to outliers with good noise-reduction capabilities and stability with respect to the regularization parameter.

Deep learning methods have shown promising results in reconstructing the susceptibility maps from the local field. These methods have the advantage of rapid and high-quality susceptibility reconstruction. DeepQSM[14] utilized a 3D-UNet model to solve the ill-posed problem at hand. The authors[14] showed that training the model on synthetic data and testing on the in-vivo data can generate marginally good susceptibility maps. QSMnet[15] is also a 3D-UNet model designed with 5x5x5 convolution filters for susceptibility mapping. The developed model was trained on in-vivo data and showed that high-quality reconstruction is possible with single orientation data. In a similar study, the authors of QSMnet+[16] have explored the linearity in susceptibility mapping by augmenting the in-vivo dataset with scaled susceptibility maps. QSMnet + has improved susceptibility imaging in the selected region of interest compared to QSMnet. Another network, QSMGAN[17] proposed adversarial training for susceptibility reconstruction. The deep learning methods discussed so far followed an ideal scenario (as shown in Fig. 1) of training/testing for QSM. A more generalizable and robust deep learning method for QSM, xQSM methods[18,19] have utilized octave convolutions for resolution agnostic and accelerated QSM reconstruction. MoDL-QSM[20] and LPCNN[21] introduced model-based iterative pipelines for QSM with alternating data consistency and deep learning based priors. Meta-learning for QSM, i.e., ICCU-Net[22] proposed a two-stage learning method for transferring

knowledge from the synthetic domain to the in vivo domain to handle limited in vivo data. Further, meta-QSM [23] introduces a weight prediction layers enabling resolution specific learning of weights and biases for susceptibility mapping. In a similar study, Oh et al. [24] introduced resolution agnostic unsupervised susceptibility mapping using adaptive instance normalization. Furthermore, Xiong et al. [25] have introduced affine transform based orientation and resolution agnostic susceptibility mapping. Similarly, recent methods [26,27,28,29,30] have shown great promise in high-quality susceptibility mapping.

Deep learning models for QSM have focused on adding advantages in the form of high-quality reconstruction, inference time, unsupervised learning, and resolution agnostic reconstruction. However, all these methods relied on advancements in deep learning. For example, xQSM [18] utilized octave convolutions, and ICCU-Net [22] adapts meta-learning. Modeling robust deep learning methods for QSM has been challenging [31], where data acquisition protocols including variability in scanner type may lead to inaccurate reconstruction maps. Techniques such as data augmentation have been successful to an extent in improving the generalizability of deep learning models for susceptibility reconstruction. Training deep learning models on large heterogenous datasets have the highest capacity to build salience and robust feature representation for handling data-driven tasks. This involves curating data from multiple centers, which is not plausible due to data privacy and security issues, especially in medical image analysis tasks. The lack of generalizability in QSM using deep learning models can be attributed to variability in the acquisition of MR images. Specifically, variations in magnetic field strength, TE (time to echo), TR (repetition time), and spatial resolution [31]. Consistent or uniform protocols across scanners are not a plausible solution. However, methods such as MoDL-QSM [20] and LPCNN [21] proposed model-based QSM pipelines for improving generalizability by utilizing the physics of QSM. Nevertheless, the learned prior or the regularizer in these methods are still deep learning based ones; hence, the problem of generalizability remains unsolved.

This work proposes a hybrid two-step reconstruction approach to improve deep learning based QSM reconstruction for a realistic scenario (as shown in Fig. 1). The susceptibility map prediction obtained from deep learning methods has been refined in the developed framework to ensure consistency with the measured local field. The extensive experiments conducted in this work have shown that the proposed method for QSM is agnostic to variations in magnetic field strength and the amount of training data. The contributions of the proposed method can be summarized as follows:

- A two-step hybrid reconstruction approach has been proposed for improving the generalizability of the deep learning based susceptibility mapping. The proposed method can be easily integrated into existing deep learning methods for QSM reconstruction, making it the most generic framework.
- The proposed two-step hybrid approach for QSM has been evaluated in different experimental settings designed on the basis of training data availability and testing data variability to showcase the efficacy.

2 | METHODS

Deep learning methods have shown promising results in reconstructing susceptibility maps from local field data obtained from the MR phase images. This section introduces existing deep learning methods and the proposed hybrid method for QSM reconstruction. Let f represent a deep model characterized by a set of parameters (or weights) θ, $(\mathrm{y}, \mathrm{x}^C)$ be the data pairs where y denotes the local field and x^C denotes the COSMOS reconstructed susceptibility map, $\mathcal{L}$ be a cost function, and N be the number of training data samples.

2.1 | Existing Methods

The existing deep learning methods for susceptibility reconstruction can be broadly categorized into (1) End-to-End deep learning methods, (2) Model based deep learning methods, and (3) Test time adaptation methods. The summary of these deep learning methods as a block diagram for QSM is shown in Fig. 2.

2.1.1 | End-to-End Deep Learning

Given a set of training data pairs $(\mathrm{y}, \mathrm{x}^C)$, the deep learning models are trained to optimize a cost function as shown in Eq. (5). The trained deep learning models are then subjected to make predictions on the test cases to reconstruct the susceptibility maps. Methods like QSMnet [15], DeepQSM [14], QSMnet+ [16], xQSM [18] etc. fall under this category.

$$\underset{\theta}{\operatorname{argmin}} \ \frac{1}{N}\sum_{i=1}^{N}\mathcal{L}\big(f(\mathrm{y}_i,\theta),\mathrm{x}_i^C\big) \tag{5}$$

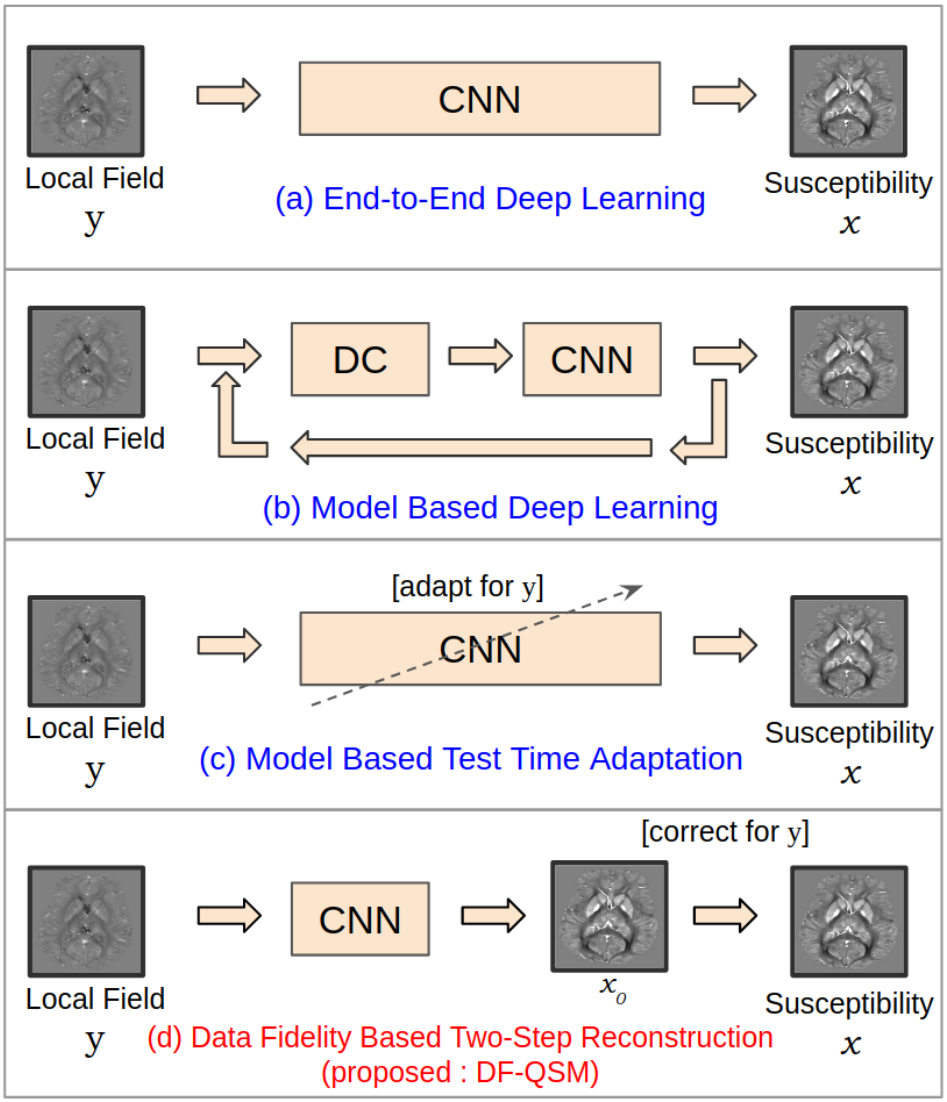

Figure 2 Overview of the deep learning based QSM reconstruction methods. (a) End-to-End deep learning methods using convolutional neural networks (CNN) such as QSMnet [15], xQSM [18] etc. (b) Model-based deep learning methods like LPCNN [21], MoDL-QSM [20], etc, with DC representing the data consistency term and CNN playing the role of proximal regularizer, (c) Test time adaptation methods like FINE [32]. (d) The proposed two-step hybrid reconstruction framework based on data fidelity for QSM (DF-QSM). The detailed description of the proposed DF-QSM framework is shown in Fig. 3.

2.1.2 | Model Based Deep Learning

Methods like MoDL-QSM [20] and LPCNN [21] use proximal gradient descent combining data consistency and a deep learning-based regularizer for effective susceptibility mapping. The iterations shown in Eq. (6) are initialized from $x_0 = 0$ and succinctly denote the final estimate x_n as $g(\mathrm{y}, \theta)$, the parameters of deep learning based regularizer are optimized as shown in Eq. (7). Model-based deep learning methods perform reasonably well under limited training data settings due to the data consistency step.

$$x_{k+1} = f(x_k - \alpha\phi^H(\phi x_k - \mathrm{y}), \theta) \tag{6}$$

$$\underset{\theta}{\operatorname{argmin}} \ \frac{1}{N}\sum_{i=1}^{N} \mathcal{L}\big(g(\mathrm{y}_i, \theta), x_i^C\big) \tag{7}$$

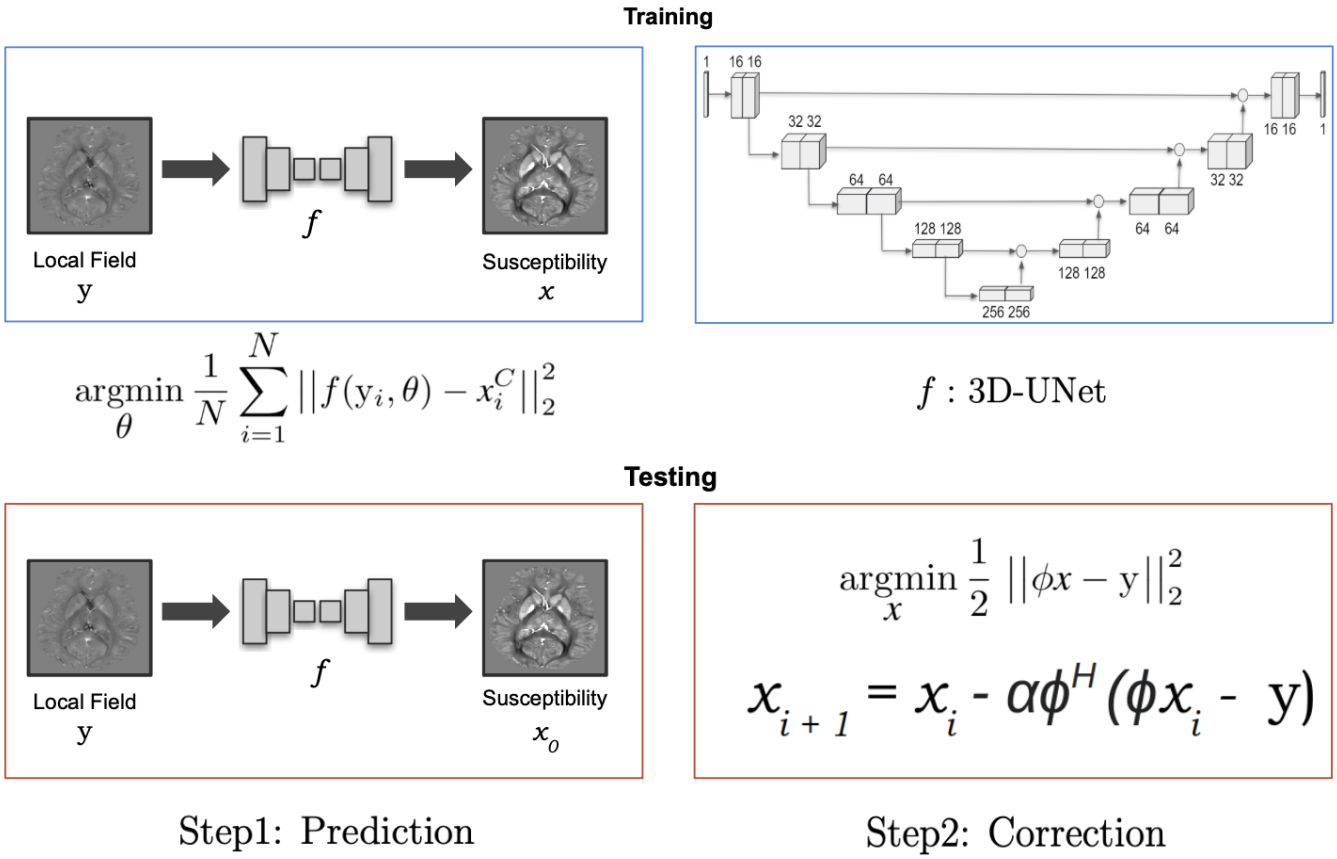

Figure 3 The training and the testing procedure of the proposed data fidelity based two-step hybrid reconstruction framework for quantitative susceptibility mapping (DF-QSM). The deep model f utilized in the proposed DF-QSM framework is a 3D-UNet architecture. The testing phase of the proposed hybrid approach framework has two steps (prediction followed by correction).

2.1.3 | Test Time Adaptation

The training process of deep learning models under this category is similar to end-to-end deep learning methods. However, to develop subject (or test volume) specific deep learning models , methods such as the fidelity-imposed network edit (FINE)[32] proposed the test time adaptation approach to tune the parameters of a trained deep model specific to the testing volume by minimizing the data consistency error as shown in Eq. (8), where W denotes the weighting matrix.

$$\underset{\theta}{\text{argmin}} \; ||W(\phi f(\mathrm{y}_{test}, \theta) - \mathrm{y}_{test})||_2^2 \tag{8}$$

2.2 | Proposed Method: DF-QSM

The proposed framework is a decoupled model based deep learning method for QSM. The deep learning model in the proposed framework is trained independently of data consistency (DC), but the output of the trained deep learning model is refined using the data fidelity during inference (test time). The proposed two-step hybrid reconstruction (DF-QSM) has been evaluated under different experimental settings, designed on the basis of training data availability and testing data variability. The training and testing procedures of the proposed two-step hybrid QSM reconstruction framework (Fig. 3) are as follows:

2.2.1 | Training

Let f represent a 3D-UNet model with four encoding and four decoding levels, as shown in Fig. 3. The numbers given for each feature block represent the number of channels (C) present in the 4D feature maps (C $\times$ Z $\times$ Y $\times$ X). Each convolution block operates using a 3 $\times$ 3 $\times$ 3 filter, followed by batch normalization and ReLU activation. Max pooling in the encoder is done with a stride of 2 $\times$ 2 $\times$ 2 and transposed convolution

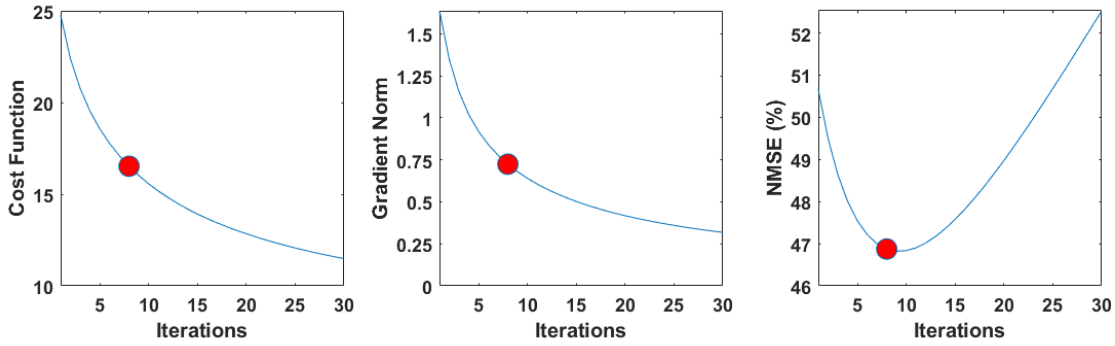

Figure 4 Analysis for the stopping criterion using the validation set in the correction stage of the proposed DF-QSM framework. The cost function is $\frac{1}{2}\ ||\phi x - y||_2^2$ and the gradient norm is $\phi^H(\phi x - y)$. The iterations are terminated as soon as the gradient norm falls below 0.75 (resembling minimum NMSE). The threshold for the gradient norm, determined through the validation set (as shown above), remains constant for all test cases in each experiment.

in the decoder is done with a filter of $2 \times 2 \times 2$ with a stride $2 \times 2 \times 2$. The circular connector represents the feature concatenation operation. The deep model f is trained by minimizing the cost function, as shown in Eq. (9). The models trained in this fashion have poor generalization, when evaluating them on the data obtained from different acquisition settings.

$$\underset{\theta}{\operatorname{argmin}} \frac{1}{N} \sum_{i=1}^{N} ||f(y_i, \theta) - x_i^C||_2^2 \tag{9}$$

2.2.2 | Testing

The testing phase of the proposed framework has two steps. As shown in Eq. (10), an initial estimate of the susceptibility map has been obtained using the trained deep model,

$$x_0 = f(y_{test}, \theta) \tag{10}$$

The initial estimate obtained in Eq. (10) was used to initialize the following minimization,

$$\underset{x}{\operatorname{argmin}} \frac{1}{2}\ ||\phi x - y_{test}||_2^2 \tag{11}$$

$$x_{k+1} = x_k - \alpha\big(\phi^H(\phi x - y_{test})\big) \tag{12}$$

The minimization shown in Eq. (11) is solved iteratively using the gradient descent update shown in Eq. (12). The initial estimate x_0 from the prediction stage of the proposed framework acts as a good starting point for optimizing the subject (testing volume) specific minimization problem shown in Eq. (11). The iterations are terminated as soon as the gradient norm falls below 0.75 (Fig. 4). The iterative updates in the gradient descent for the proposed DF-QSM include implicit regularization, which is achieved by controlling the number of iterations. Consequently, if a higher number of iterations is used, DF-QSM exhibits the risk of overfitting the data, similar to the trends reported in [12] for iterative refinement of susceptibility maps without explicit regularization. To mitigate this risk of overfitting, an early stopping criterion is employed that helps in preventing unnecessary iterations, ensures a balance between convergence, and avoids fitting noise or irrelevant details in the reconstructed images. The gradient norm threshold is pre-established using the validation set and remains consistent across all test cases in every experiment.

The two-step hybrid approach presented in this study (DF-QSM) shares similarities with the study conducted by Lambert et al. (referred to as HD-QSM)[13]. The HD-QSM approach also consists of a two-step procedure, in which it initially aims to find a solution using an L1 norm based linear data consistency approach and then employs this solution as an initial estimate for an L2-norm based linear data consistency method. In contrast, the proposed DF-QSM approach utilizes a pre-trained deep learning model for the initial prediction of susceptibility, subsequently employing this prediction as an initialization for the L2-norm based linear data consistency step. The proposed approach also shares similarities with the testing phase correction approach, DL with L2 regularization (DLL2)[33]. Both approaches initially compute an initial estimate of the susceptibility map using the trained deep model using Eq. (10). However, in the case of DLL2, an improved estimate for the susceptibility map is obtained by the minimization problem shown in Eq. (13).

$$x_{DLL2} = \underset{x}{\operatorname{argmin}}\ ||W\ (\phi x - y_{test})\ ||_2^2 + \lambda||x - x_0||_2^2, \tag{13}$$

The solution for the updated susceptibility map was then computed analytically. Both the approaches differ in terms of minimization problem as well as the implementation. In contrast to utilizing the initial estimate from the deep learning model in the regularization term (like in DLL2, Eq. (13)) ensuring proximity of the solution, the proposed DF-QSM uses it as the initial guess for the gradient descent update as shown in Eq. (12). In addition, DLL2 adopts an analytical expression with regularization parameter λ to acquire the refined susceptibility map, in contrast to the iterative implementation that uses gradient descent update steps, where the number of iterations serves as implicit regularization in the proposed DF-QSM. By utilizing the initial estimate from the deep learning model as the starting point for the susceptibility map in the gradient descent update, the proposed approach benefits from a more informed and accurate initialization. This can lead to a faster convergence and improved reconstruction accuracy. The proposed approach directly leverages the output of the deep learning model as an initial estimate of the susceptibility map. This direct integration of deep learning information has been shown to exploit the learned features of the model more effectively in QSM reconstruction.

3 | EXPERIMENTS

3.1 | Datasets

In this study, three benchmark datasets were considered to show the efficacy of the proposed approach. Dataset I [15] consisted of 60 scans taken at 3 Tesla from twelve healthy subjects using Siemens Healthineers, Forchheim, Germany's Tim Trio (nine subjects), and MAGNETOM Skyra (three subjects). A 3D single echo gradient echo (GRE) sequence with the following settings was used to acquire the scans at five different head orientations: voxel size of 1×1×1 mm^3, TR of 33 ms, TE of 25 ms, bandwidth of 100 $Hz/pixel$, and flip angle of 15°. Tim Trio and Skyra scans have their field of view (FOVs) set to 256×224×176 mm^3 and 224×224×176 mm^3, respectively. The matrix size of 176 ×176×160 was constant across all volumes present in the dataset. Eight healthy subjects scans from four distinct head orientations at 7 Tesla (Philips Achieva) made up Dataset-II [21], which produced 32 volumes. Three different 3D GRE sequences with a voxel size of 1×1×1 mm^3 were used to acquire the data. The first four subjects had the following sequence parameters: five echoes, a FOV of 224×224×126 mm^3, a TR of 28 ms, and a TE1/δTE of 5/5 ms. TR of 45 ms, TE1/δTE of 2/2 ms, nine echoes, and FOV of 224×224×110 mm^3 were the parameters for the next three individuals. The final subject had a FOV of 224×224×110 mm^3, a TR of 45 ms, and a TE1/δTE of 2/2 ms with 16 echoes. Of these, 16 volumes had a matrix size of 224×224×126, and the other 16 volumes had a matrix size of 224×224×110. To evaluate the proposed method on the dataset with different resolution, the proposed method was tested on the subject with hemorrhage [20], whose data was captured using 3T MR scanner with matrix size: 256×256×66 and voxel size: 0.86×0.86×2 mm^3.

3.2 | Experimental Studies

The data pairs, i.e., the input local field and the COSMOS label maps that match the input local field orientation, were used to train all the deep learning models considered in this work. Similar data augmentation techniques used in Ref. [15] were also used here to increase the training data. All deep learning models were trained on $64 \times 64 \times 64$ three-dimensional patches. Across all the experimental studies, the models were trained on training subjects from Dataset I. The models were tested on testing subjects from Dataset I. Further, the Dataset II was entirely used for testing. The experimental details are as follows:

3.2.1 | Study 1 (Maximum Data Training)

The aim of this experimental setup was to evaluate the generalizability of deep learning models for QSM in maximum data training settings. The deep learning models considered in this study were trained using five subjects with 25 scans from Dataset I. Training subjects were chosen in a similar way to those of QSMnet [15]. In this experimental study, the deep models were evaluated as:

(a) The trained deep learning models were evaluated on the six testing subjects with 30 scans of Dataset I similar to the QSMnet study [15].

(b) Furthermore, deep learning models were also tested on Dataset II (eight subjects with 32 scans) captured under different acquisition settings.

3.2.2 | Study 2 (Limited Data Training)

The aim of this experiment was to evaluate the generalizability of deep learning models for QSM under limited data training settings. The deep learning models considered in this study were trained using one subject with 5 scans from Dataset I. The training process was repeated five times by changing the training subject. Training subjects were chosen similar to QSMnet study [15]. The evaluation metrics were averaged from five single-subject-trained models. In this experimental study the deep models were evaluated as:

Table 1 Quantitative metrics (mean ± std) of the reconstructed susceptibility maps for experimental study 1. The best results are shown in bold. Compared to the second-best-performing model (LPCNN), statistically significant results ($P < 0.05$) from the two-tailed t test (Welch test) were shown with *.

Testing Dataset	Dataset I				Dataset II			
Experiment	Study 1(a)				Study 1(b)			
Model | Metric	SSIM ↑	PSNR (dB)↑	NMSE (%) ↓	HFEN (%) ↓	SSIM ↑	PSNR (dB) ↑	NMSE (%) ↓	HFEN (%) ↓
QSMnet	0.910 ± 0.01	41.04 ± 1.01	51.39 ± 3.81	48.41 ± 4.42	0.928 ± 0.01	32.98 ± 1.72	61.78 ± 3.32	56.43 ± 4.49
xQSM	0.908 ± 0.01	40.98 ± 1.03	52.23 ± 3.78	50.43 ± 4.66	0.928 ± 0.01	33.10 ± 1.83	61.68 ± 3.34	57.54 ± 4.50
3D-UNet	0.910 ± 0.01	41.10 ± 0.93	51.19 ± 3.39	49.21 ± 3.82	0.928 ± 0.01	33.07 ± 1.75	61.64 ± 3.28	57.27 ± 4.49
LPCNN	0.905 ± 0.01	40.88 ± 1.06	52.93 ± 4.01	49.71 ± 4.78	0.929 ± 0.01	33.09 ± 1.79	57.83 ± 3.88	55.14 ± 4.36
FINE	0.909 ± 0.01	41.07 ± 0.91	51.40 ± 3.37	49.43 ± 3.81	0.928 ± 0.01	33.14 ± 1.78	61.94 ± 3.33	57.80 ± 4.61
DF-QSM (proposed)	**0.919 ± 0.01***	**41.58 ± 0.99***	**49.08 ± 4.15***	**46.76 ± 4.87***	**0.935 ± 0.01**	**33.36 ± 1.88**	**55.99 ± 5.27**	**54.07 ± 5.64**

(a) The trained deep learning models were evaluated on the six testing subjects with 30 scans from Dataset I similar to the study QSMnet[15].

(b) Furthermore, deep learning models were also tested on Dataset II (eight subjects with 32 scans) captured under different acquisition settings.

3.3 | Comparison Methods

The proposed approach (DF-QSM) was evaluated under various experimental conditions and compared with deep architecture benchmarking for QSM. Specifically, the proposed method was compared with deep learning methods QSMnet[15], xQSM[18], and 3D-UNet (Fig. 3), model based deep learning method LPCNN[21], and test time adaptation method FINE[32]. To have a fair comparison between FINE and the proposed DF-QSM, 3D-UNet shown in Fig. 3 was utilized in FINE.

3.4 | Implementation

The 3D-UNet considered in this work was trained using the PyTorch framework[34]. The 3D-UNet parameters in all experimental studies were optimized using the Adam optimizer[35]. The initial learning rate was $5e^{-4}$ and was decayed by 0.1 once training completes for 50% and 75% of total epochs. The size of the mini-batch considered was 16. The total number of epochs was fixed at 25 in all experiments. Step length α was set empirically equal to 1. In all experiments to augment the training dataset, the COSMOS QSM maps were subjected to rotational transformations within an angle range of -45 to +45 degrees relative to B0, and local field maps were subsequently generated through dipole convolution. To quantify the performance of the deep learning model, the standard merit figures for QSM[36], such as structural similarity index (SSIM), normalized mean square error (NMSE), and high frequency error norm (HFEN), were calculated in all experiments. All computations performed in this work, including the training of deep learning models, used a Linux workstation with i9 9900X (CPU), 128 GB RAM, and two NVIDIA Quadro RTX 8000 GPU cards that have a memory of 48GB each.

4 | RESULTS

4.1 | Study 1 (Maximum Data Training)

The performance metrics from the study 1 were detailed in Table 1. As shown in Table 1, across all methods, the proposed hybrid method outperformed the existing deep learning models for QSM. A similar trend was observed when the generalizability of deep learning models in Dataset II obtained under different acquisition settings was evaluated. The representative results from study 1 were shown in Fig. 5 (study 1(a)) and Fig. 6 (study 1(b)). The improvements in reconstruction quality in the proposed iterations on the sample axial slices (study 1(b) shown in Fig. 6) were shown in Fig. 7. The correlation coefficient, coefficient of determination, and slope of the scatter plots were improved across iterations.

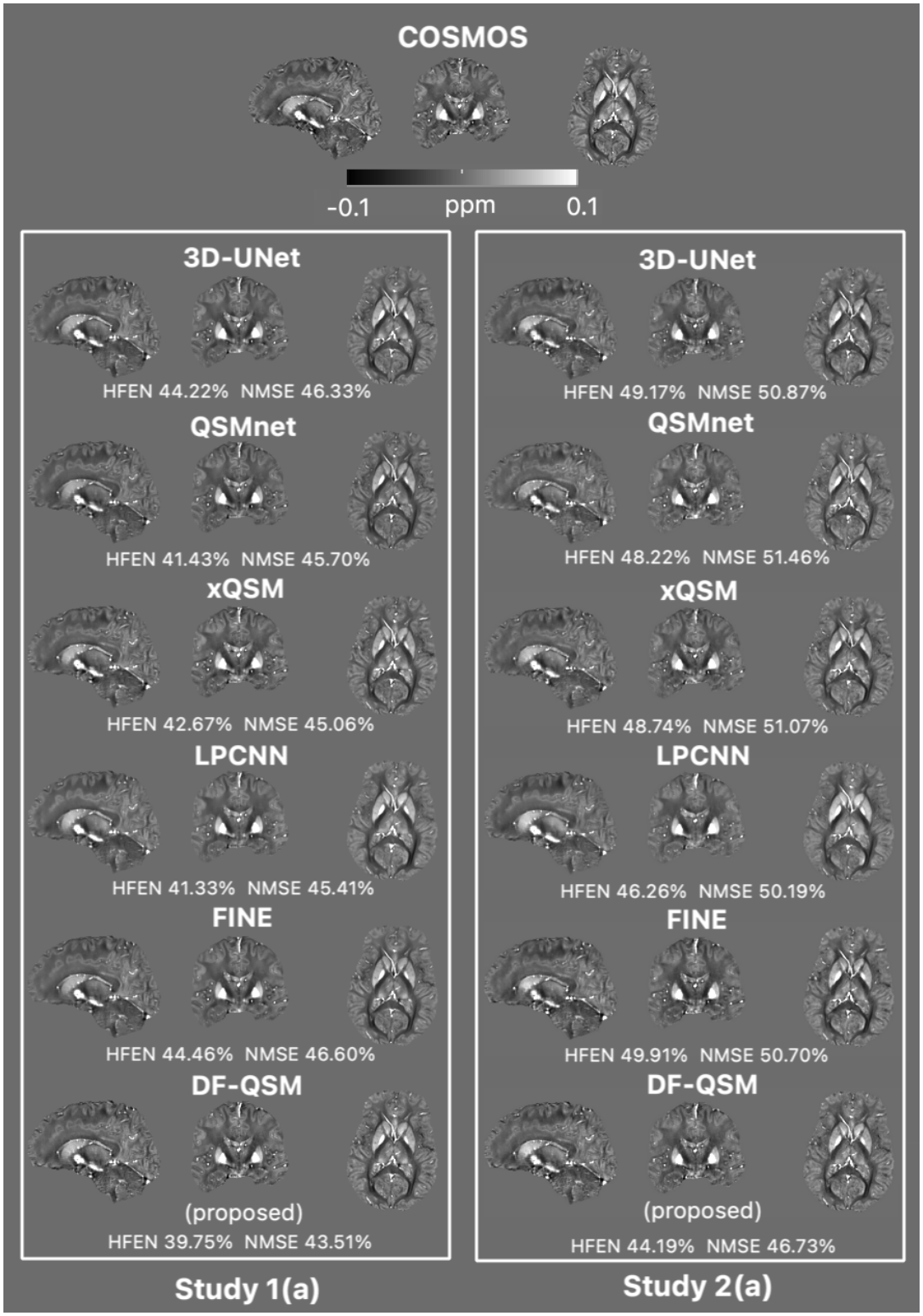

Figure 5 Quantitative susceptibility maps of the sample test volume from Dataset I. The experimental details of the deep learning models were given in study 1(a) and study 2(a). The NMSE (%) and HFEN (%) of the test volumes with respect to COSMOS were given below for each of the reconstruction methods.

Table 2 Quantitative metrics (mean ± std) of the reconstructed susceptibility map for experimental study 2. The metrics were averaged over five different runs conducted in the study. The best results are shown in bold. Compared to the second best performing model (LPCNN), statistically significant results ($P < 0.05$) of the two-tailed t test (Welch test) were shown with *.

Testing Dataset	**Dataset I**				**Dataset II**			
Experiment	**Study 2(a)**				**Study 2(b)**			
Model | Metric	**SSIM** ↑	**PSNR** (dB)↑	**NMSE** (%) ↓	**HFEN** (%) ↓	**SSIM** ↑	**PSNR** (dB) ↑	**NMSE** (%) ↓	**HFEN** (%) ↓
QSMnet	0.891 ± 0.01	40.21 ± 1.19	57.24 ± 4.96	55.32 ± 5.59	0.920 ± 0.01	33.07 ± 1.77	65.27 ± 3.14	60.93 ± 4.28
xQSM	0.892 ± 0.01	40.09 ± 1.03	57.42 ± 3.78	55.78 ± 4.56	0.919 ± 0.01	32.98 ± 1.69	65.52 ± 3.10	61.37 ± 4.10
3D-UNet	0.892 ± 0.01	40.15 ± 1.01	57.10 ± 4.01	56.41 ± 4.64	0.920 ± 0.01	33.01 ± 1.72	65.43 ± 2.86	61.76 ± 3.87
LPCNN	0.898 ± 0.01	40.44 ± 1.06	56.27 ± 3.97	53.28 ± 4.62	0.923 ± 0.01	33.10 ± 1.75	60.36 ± 3.80	58.38 ± 4.20
FINE	0.897 ± 0.01	40.30 ± 0.95	57.13 ± 3.90	56.63 ± 4.51	0.924 ± 0.01	**33.42 ± 1.76**	64.16 ± 3.62	62.51 ± 4.25
DF-QSM (proposed)	**0.905 ± 0.01***	**40.78 ± 1.04***	**53.70 ± 4.70***	**52.83 ± 5.53**	**0.930 ± 0.01***	33.33 ± 1.87	**58.16 ± 4.75***	**57.11 ± 5.18***

4.2 | Study 2 (Limited Data Training)

The performance metrics from the study 2 were detailed in Table 2. As shown in Table 2, in all methods, the proposed method outperformed the existing deep learning models for QSM. Specifically, the improvements in terms of SSIM, PSNR, and NMSE were statistically significant compared to the second-best performing model LPCNN. A similar trend was observed when evaluated for the generalizability of deep learning models on Dataset II obtained under different acquisition settings. The representative reconstruction results from study 2 were shown in Fig. 5 (Study 2(a)) and Fig. 6 (Study 2(b)) respectively.

4.3 | Susceptibility Region of Interest Analysis

The representative region of interest (ROI) analysis on a sample test volume from Dataset I was performed for three different local regions as highlighted in Fig. 8 (a). The scatter plots of reconstructed susceptibility values of different model based methods such as LPCNN, FINE, DLL2, and the proposed DF-QSM versus that of COSMOS were shown in Fig. 8 (b). The scattered data points in Fig. 8 were marked with different colors to distinguish between brain regions. These plots confirm the superiority of the proposed method. This was also obvious from the correlation coefficient and the coefficient of determination of the proposed method compared to LPCNN. The mean and standard deviation (across five different head orientations) of these local regions obtained using LPCNN, FINE, DLL2, and the proposed DF-QSM were compared with that of COSMOS in Fig. 8 (c).

4.4 | DF-QSM with Existing Deep Learning Methods

Performance comparison of the proposed framework on the existing deep learning methods for QSM was shown in Table 3. The deep learning model (3D-UNet) used in the proposed framework was replaced by QSMnet, LPCNN and FINE, for this experiment. As shown in Table 3, the proposed method has shown a similar trend in improving the end-to-end deep learning method 'QSMnet,' model based deep learning method 'LPCNN,' and test time adaptation method 'FINE'. This also affirms that the proposed methodology can be utilized with other CNN based models to improve the QSM reconstruction, making it the most generalizable method compared to existing methods.

4.5 | Comparison with Conventional Reconstruction Methods

The proposed method was also compared with conventional susceptibility reconstruction methods. Specifically, L2[8], TKD[7], MR-TKD[37], NDI[12], FANSI[38] and DLL2[33] were compared (Table 4 and Fig. 9) on Dataset I. As shown in the Table 4 and Fig. 9, the proposed DF-QSM has shown better reconstruction compared to existing conventional methods.

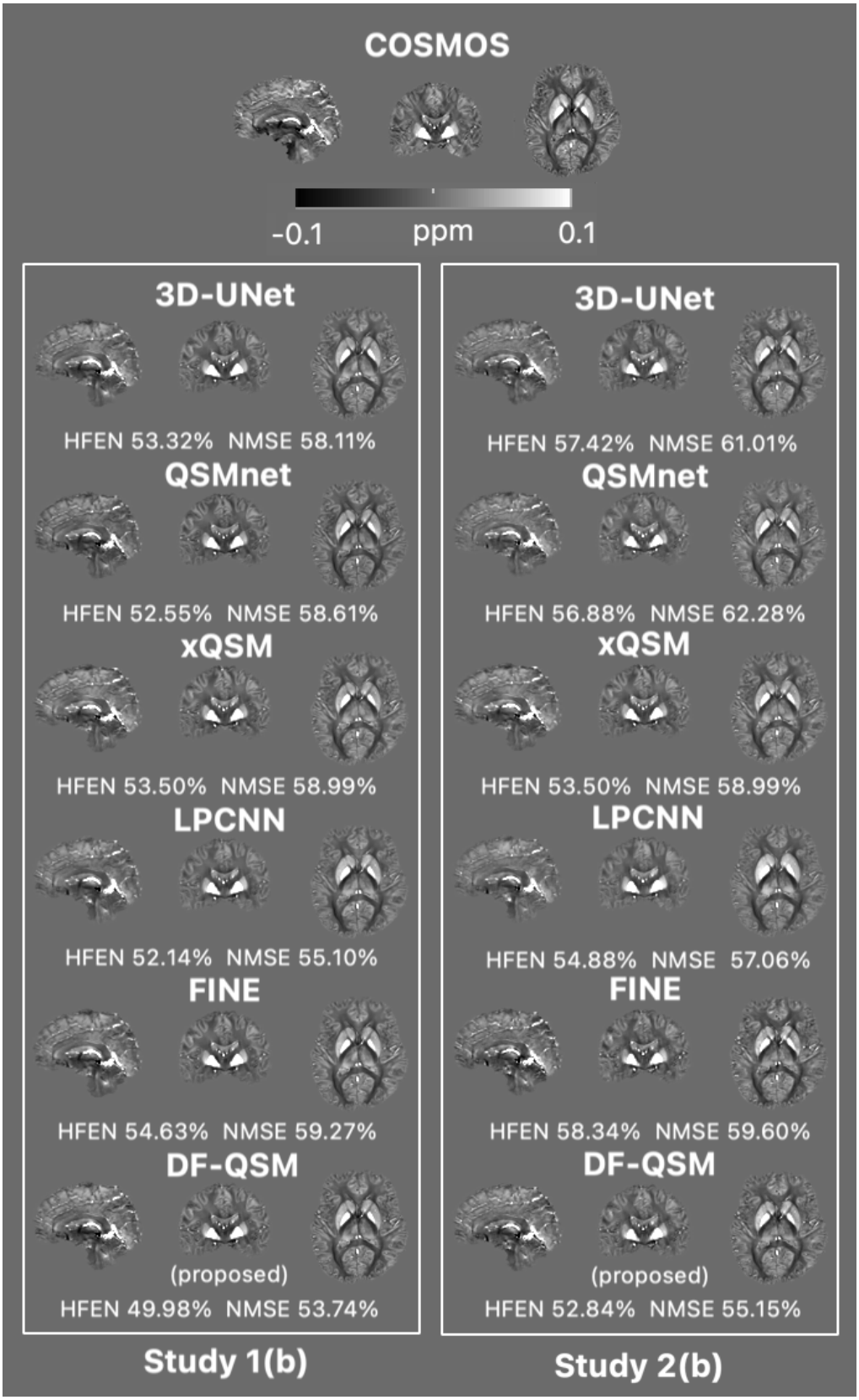

Figure 6 Quantitative susceptibility maps (axial view) and difference images (with respect to COSMOS) of the sample test volume from Dataset II. The experimental details of the deep learning models were given in study 1(b) and study 2(b). The NMSE (%) and HFEN (%) of the test volumes with respect to COSMOS were given below for each of the reconstruction methods.

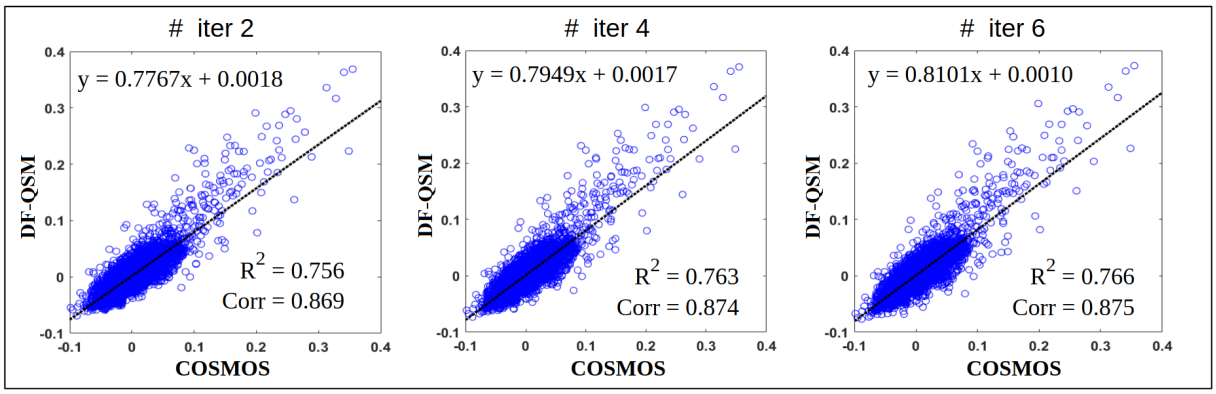

Figure 7 The improvement in reconstruction quality across iterations of the proposed DF-QSM method for the sample axial slice shown in Fig. 4.

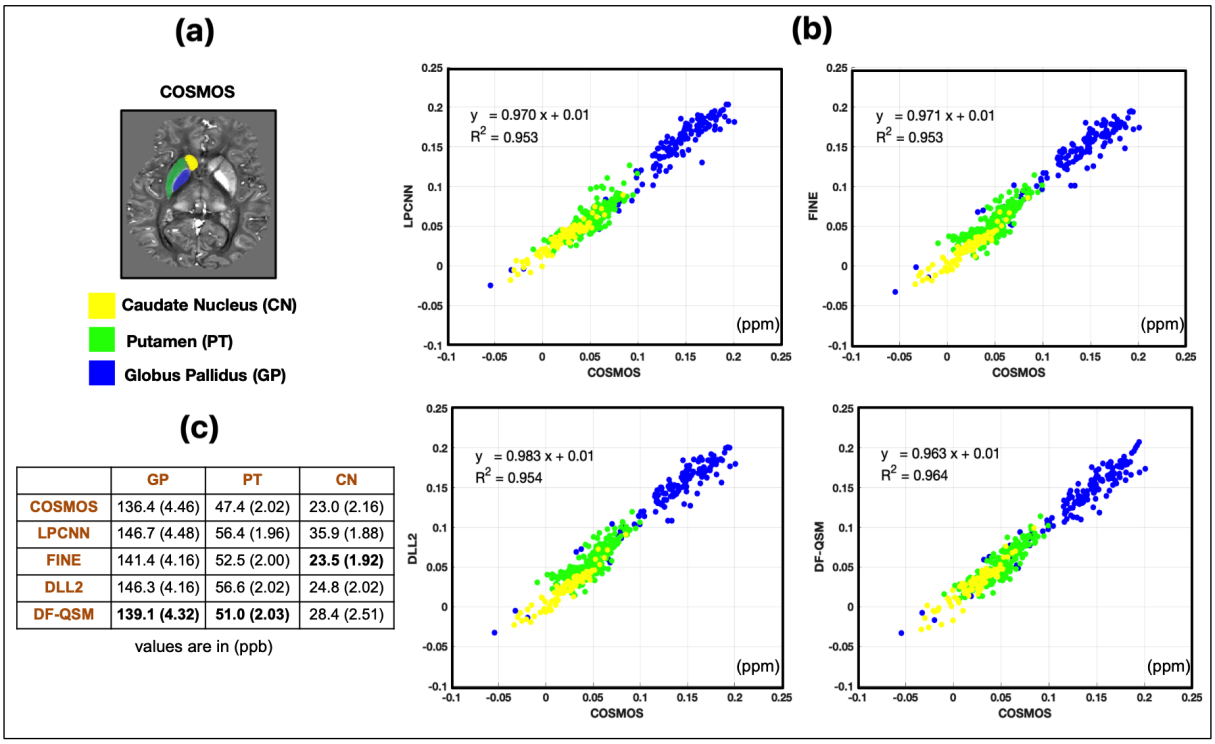

(c)

	GP	PT	CN
COSMOS	136.4 (4.46)	47.4 (2.02)	23.0 (2.16)
LPCNN	146.7 (4.48)	56.4 (1.96)	35.9 (1.88)
FINE	141.4 (4.16)	52.5 (2.00)	**23.5 (1.92)**
DLL2	146.3 (4.16)	56.6 (2.02)	24.8 (2.02)
DF-QSM	**139.1 (4.32)**	**51.0 (2.03)**	28.4 (2.51)

values are in (ppb)

Figure 8 Region of interest (ROI) analysis performed using model based/hybrid QSM methods. (a) COSMOS map with ROIs highlighted, (b) Scatter plots of the susceptibility values in reference to the COSMOS, and (c) mean and standard deviations of the considered local regions in (ppb) across five orientations.

4.6 | Performance Comparison on Dataset with Hemorrhage

To evaluate the proposed method on a dataset with different resolution, the proposed method was tested on the subject with hemorrhage [20] (the dataset details were given in Sec. 3.1.). The axial views of the reconstructed susceptibility maps using Star-QSM [39], LPCNN, FINE, DLL2, and DF-QSM were displayed in Fig. 10. Since the COSMOS acquisitions were not available in this case, the local field was re-computed using the forward operator and was then compared with the given local field. As, shown in Fig. 10, the proposed method yielded a better reconstruction compared to the existing methods.

Table 3 Performance comparison of the proposed framework on the existing deep learning methods for QSM. The experimental details were given in study 2. The deep learning model (3D-UNet) used in the proposed DF-QSM framework was replaced by QSMnet, LPCNN, and FINE for this experiment. The best results were shown in bold.

Testing Dataset	Dataset I				Dataset II			
Experiment	Study 2(a)				Study 2(b)			
Model | Metric	SSIM ↑	PSNR (dB)↑	NMSE (%) ↓	HFEN (%) ↓	SSIM ↑	PSNR (dB) ↑	NMSE (%) ↓	HFEN (%) ↓
QSMnet	0.891 ± 0.01	40.21 ± 1.01	57.24 ± 4.96	55.32 ± 5.59	0.920 ± 0.01	33.07 ± 1.77	65.27 ± 3.14	60.93 ± 4.28
QSMnet + DF-QSM	**0.906 ± 0.01**	**40.90 ± 1.10**	**53.41 ± 4.98**	**51.93 ± 6.01**	**0.931 ± 0.01**	**33.39 ± 1.88**	**57.92 ± 5.01**	**56.65 ± 5.49**
LPCNN	0.898 ± 0.01	40.44 ± 1.06	56.27 ± 3.97	53.28 ± 4.62	0.923 ± 0.01	33.10 ± 1.75	60.36 ± 3.80	58.38 ± 4.20
LPCNN + DF-QSM	**0.908 ± 0.01**	**40.92 ± 1.09**	**53.77 ± 5.15**	**51.45 ± 6.07**	**0.932 ± 0.01**	**33.31 ± 1.85**	**56.79 ± 5.16**	**55.33 ± 5.49**
FINE	0.897 ± 0.01	40.30 ± 0.95	57.13 ± 3.90	56.63 ± 4.51	0.924 ± 0.01	33.42 ± 1.76	64.16 ± 3.62	62.51 ± 4.25
FINE + DF-QSM	**0.905 ± 0.01**	**40.80 ± 1.01**	**54.68 ± 5.05**	**53.76 ± 6.01**	**0.931 ± 0.01**	**33.57 ± 1.85**	**59.11 ± 4.90**	**58.31 ± 5.43**

Table 4 Performance comparison of the proposed framework with conventional QSM reconstruction methods. The metrics were averaged over 30 test volumes from Dataset I. The best reporting results were shown in bold.

Method | Metric	SSIM ↑	PSNR (dB)↑	NMSE (%) ↓	HFEN (%) ↓
L2	0.876 ± 0.02	37.70 ± 1.30	76.67 ± 8.05	66.48 ± 7.68
TKD	0.850 ± 0.02	38.51 ± 1.01	73.34 ± 7.13	67.47 ± 8.59
MR-TKD	0.882 ± 0.02	39.35 ± 1.03	64.98 ± 5.29	60.87 ± 5.87
NDI	0.877 ± 0.02	38.99 ± 1.07	66.56 ± 5.98	62.41 ± 5.32
FANSI	0.888 ± 0.01	39.50 ± 1.21	65.05 ± 7.53	59.11 ± 6.97
DLL2 (Study 2(a))	0.896 ± 0.01	40.29 ± 1.01	56.43 ± 4.04	56.03 ± 4.72
DLL2 (Study 1(a))	0.913 ± 0.01	41.22 ± 0.92	50.72 ± 3.40	48.86 ± 3.90
DF-QSM (proposed: Study 2(a))	0.905 ± 0.01	40.78 ± 1.04	53.70 ± 4.70	52.83 ± 5.53
DF-QSM (proposed: Study 1(a))	**0.919 ± 0.01**	**41.58 ± 0.97**	**49.08 ± 4.10**	**46.76 ± 4.80**

4.7 | Computation and Inference Analysis

A comprehensive comparison of the key characteristics of the proposed hybrid model (DF-QSM) for susceptibility mapping was shown in Table 5. This evaluation includes parameters, model size, and inference time. In particular, the findings reveal that the proposed DF-QSM model excels in delivering high-quality susceptibility maps while incurring only a minimal, practically negligible increase in computational time during the inference stage. This demonstrates the effectiveness of the model in maintaining computational efficiency without compromising the quality of its output, making it a promising solution for susceptibility mapping tasks.

5 | DISCUSSION

Automated susceptibility mapping is of crucial interest in MR based quantitative imaging. Conventional QSM methods relied on classical signal processing techniques for closed-form and iterative solutions. Deep learning based methods in QSM have shown a great promise especially in terms of improved reconstructed image quality and the computational advantage. However, the existing deep learning models for QSM had an inherent bias toward the distribution of training data. As a result, the generalization towards completely unseen data was minimal. As shown in the results section, on top of existing deep learning models across different experimental studies, the proposed method clearly provides a significant improvement in reconstruction quality and correlation analysis (refer to Figs. 5, 6, 8, and 9). The proposed method can generalize well to unseen test cases in limited data environments for susceptibility mapping. The same is evident from the limited data training and generalizability studies

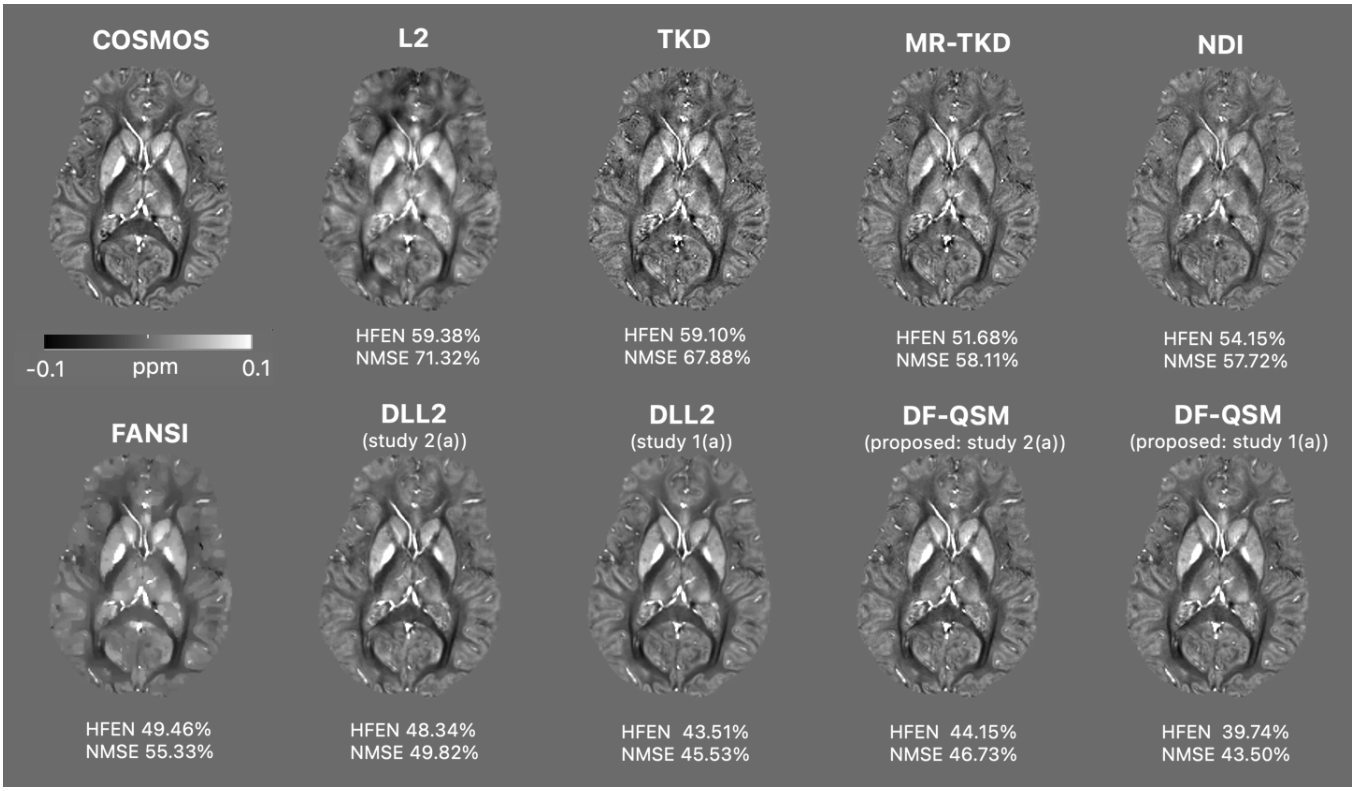

Figure 9 Quantitative susceptibility maps of the sample test volume from Dataset I. The NMSE (%) and HFEN (%) of the test volumes with respect to COSMOS were given below for each of the reconstruction methods.

Table 5 Deep learning models for QSM reconstruction: Comparison in terms of parameters (in million), model size (megabytes), and inference time (in seconds).

Model | Metric	Parameters (M)	Model Size (MB)	Inference (s) CPU	GPU
QSMnet	99.45	379.38	12.35 ± 1.36	1.52 ± 0.65
xQSM	5.21	19.89	15.25 ± 1.28	0.84 ± 0.12
LPCNN	0.47	1.7	24.35 ± 1.56	3.72 ± 0.05
3D-UNet	5.64	21.54	3.80 ± 0.05	0.28 ± 0.65
FINE	5.64	21.54	285.35 ± 3.25	90.25 ± 1.25
DF-QSM (proposed)	5.64	21.54	8.80 ± 0.05	1.28 ± 0.05

performed in this work (Table 2). While the primary goal remains to enhance performance in scenarios with restricted training data, DF-QSM has demonstrated statistically significant improvements, even in maximum data settings. This suggests that the benefits of the method extend beyond overcoming data scarcity, making it a valuable enhancement across a spectrum of data availability (Table 1 and Table 2). Moreover, the DF-QSM exhibits robustness in the face of diverse acquisition protocols, including variations in resolution settings (Fig. 10) and across different scanners (Table 1 and Table 2). This versatility is particularly crucial in real-world applications where imaging conditions can vary widely.

The existing generalizable deep learning models for QSM are based on model based frameworks. Specifically, MoDL-QSM [20] and LPCNN [21] alternate between the data consistency blocks and deep learning based priors. MoDL-QSM [20] reasonably improved the performance of susceptibility mapping but having a deep model for learning the prior limits the generalizability (MoDL-QSM [20] improves over QSMnet [15] by less than $\sim 1\%$ in NMSE and HFEN, refer to Table 1 in [20]). Furthermore, methods such as FINE [32] proposed a test-time adaptation approach to tune the parameters of the deep model specific to the test sample by minimizing the error in data consistency. The performance of FINE was slightly sub-optimal (in

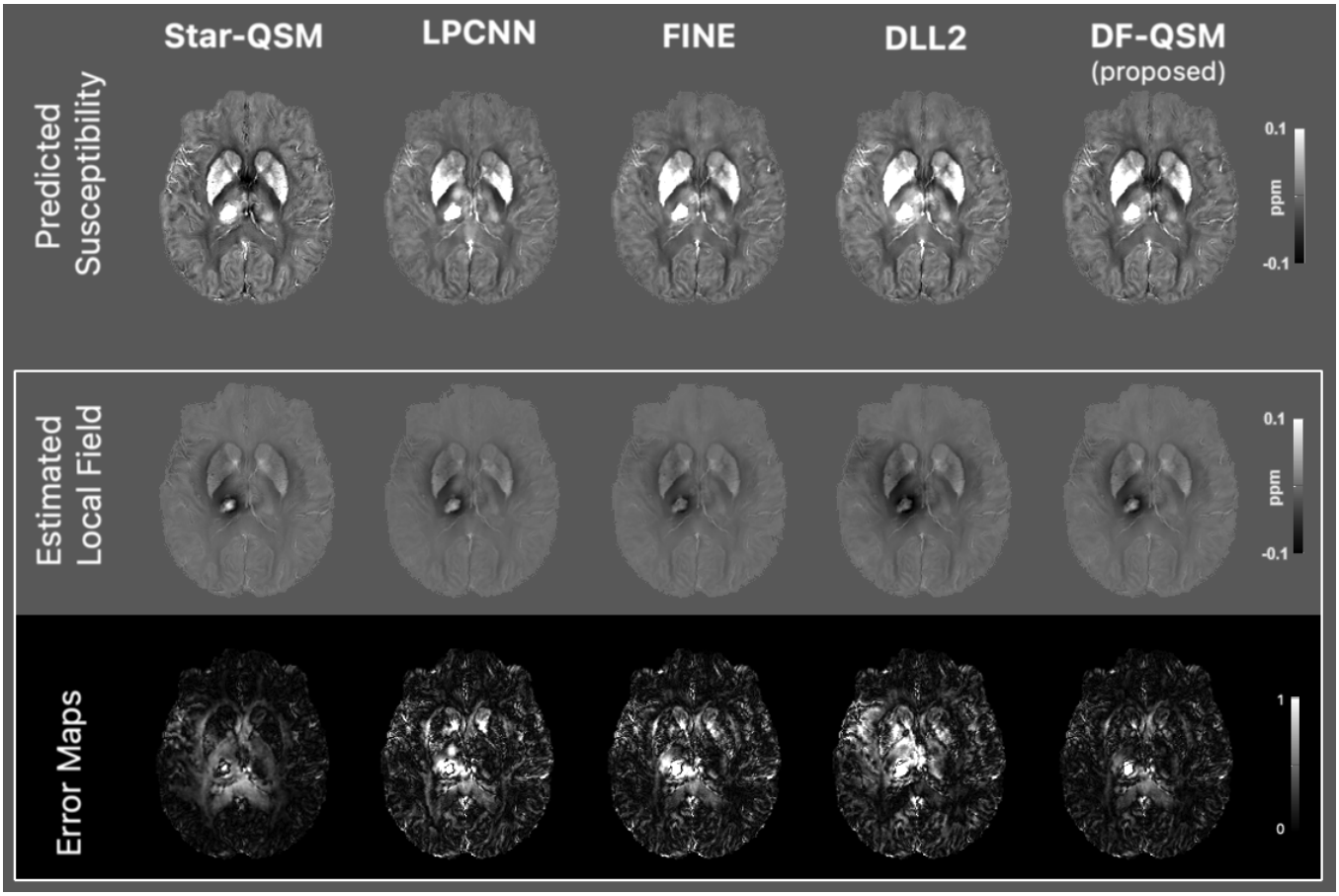

Figure 10 Quantitative susceptibility maps of the sample test volume with hemorrhage[20].

terms of NMSE and HFEN) and was on par (in terms of SSIM and PSNR) compared to LPCNN across the experimental studies. FINE relies significantly on the initial state of the trained model weights, and its focus on adjusting these weights based on data fidelity during inference introduces complexities or challenges that affect its overall performance. Further, in the experiments study 2(a) and study 2(b), the evaluation metrics were averaged from five single-subject-trained models, making it even challenging for FINE. Despite this, FINE offered reliable consistency using subject specific data fidelity optimization. However, the hyperparameters and the computation overhead are the bottlenecks for clinical adaptability of FINE (see the inference analysis in Table 5). On the contrary, this work proposed a two-step hybrid reconstruction method based on data fidelity with minimal computation (see inference analysis in Table 5) that can be easily embedded in existing deep learning models (see Table 3) for highly generalizable susceptibility mapping.

The proposed method marginally increases the computational burden for improving the initial reconstruction obtained from deep learning models. The final estimate of the reconstruction is highly dependent on the initial estimate obtained from the deep model. The initial estimate will be of good quality if the deep learning model is trained on a large amount of data and testing volume being captured under similar acquisition conditions. The proposed method has a significant advantage when the initial estimate is of poor quality, such as the initial estimates coming from deep learning models trained on limited training data or the testing volume captured from different acquisition settings (refer to Table 2 and Fig. 5 Study 2(a)). Furthermore, compared to the existing FINE test time adaptation method, the computational cost of the proposed framework was much less since the proposed framework does not require iterative updation of the network parameters. The developed source codes were released to enthusiastic users at the URL[40].

6 | CONCLUSION

This work introduced a two-step hybrid reconstruction method based on data fidelity to improve the quality of susceptibility mapping using deep learning. The proposed hybrid method was shown to be generalizable across scanning protocols and acquisitions. The proposed hybrid method

was also shown to easily integrate with well-known deep learning models to deliver increased performance/generalization independent of data properties. The proposed hybrid method DF-QSM offers a reliable and effective deep learning framework for improved quantitative susceptibility mapping. It also addresses the challenges associated with deep learning based QSM of the brain, ultimately leading to more accurate and reliable QSM images.

ACKNOWLEDGEMENTS

The authors are thankful to Dr. Jongho Lee, Laboratory for Imaging Science and Technology, Department of Electrical and Computer Engineering, Seoul National University, Seoul, South Korea, for providing the data (Dataset I). The authors are also thankful to Dr. Jeremias Sulam, Biomedical Engineering Department, Johns Hopkins University for making their data (Dataset II)[21] publicly available.

DATA/CODE AVAILABILITY

Dataset I (from the study QSMnet[15]) was made available to the authors by Prof. Lee (e-mail: jonghoyi@snu.ac.kr) of Department of Electrical and Computer Engineering, Seoul National University. Dataset II was publicly shared by the study LPCNN[21]. The codes on this manuscript will be publicly shared at the url[40].

FUNDING INFORMATION

This work was supported by S. Ramachandran-National Bioscience Award for Career Development awarded by Department of Biotechnology, Govt. of India. This work was also supported partly by the Prime Minister's Research Fellowship (PMRF), and the WIPRO-GE Collaborative Laboratory on Artificial Intelligence in Healthcare and Medical Imaging.

CONFLICT OF INTEREST

The authors declare no potential conflict of interest.

References

1. Vinayagamani S, Sheelakumari R, Sabarish S, et al. Quantitative susceptibility mapping: technical considerations and clinical applications in neuroimaging. *Journal of Magnetic Resonance Imaging* 2021; 53(1): 23–37.

2. Haacke EM, Liu S, Buch S, Zheng W, Wu D, Ye Y. Quantitative susceptibility mapping: current status and future directions. *Magnetic resonance imaging* 2015; 33(1): 1–25.

3. Liu C, Wei H, Gong NJ, Cronin M, Dibb R, Decker K. Quantitative susceptibility mapping: contrast mechanisms and clinical applications. *Tomography* 2015; 1(1): 3–17.

4. Wang Y, Spincemaille P, Liu Z, et al. Clinical quantitative susceptibility mapping (QSM): Biometal imaging and its emerging roles in patient care. *Journal of magnetic resonance imaging* 2017; 46(4): 951–971.

5. Deistung A, Schweser F, Wiestler B, et al. Quantitative susceptibility mapping differentiates between blood depositions and calcifications in patients with glioblastoma. *PloS one* 2013; 8(3): e57924.

6. Liu T, Spincemaille P, De Rochefort L, Kressler B, Wang Y. Calculation of susceptibility through multiple orientation sampling (COSMOS): a method for conditioning the inverse problem from measured magnetic field map to susceptibility source image in MRI. *Magnetic Resonance in Medicine: An Official Journal of the International Society for Magnetic Resonance in Medicine* 2009; 61(1): 196–204.

7. Shmueli K, Zwart dJA, Gelderen vP, Li TQ, Dodd SJ, Duyn JH. Magnetic susceptibility mapping of brain tissue in vivo using MRI phase data. *Magnetic Resonance in Medicine: An Official Journal of the International Society for Magnetic Resonance in Medicine* 2009; 62(6): 1510–1522.

8. Bilgic B, Chatnuntawech I, Fan AP, et al. Fast image reconstruction with L2-regularization. *Journal of magnetic resonance imaging* 2014; 40(1): 181–191.

9. Schweser F, Deistung A, Sommer K, Reichenbach JR. Toward online reconstruction of quantitative susceptibility maps: superfast dipole inversion. *Magnetic resonance in medicine* 2013; 69(6): 1581–1593.

10. Liu J, Liu T, Rochefort dL, et al. Morphology enabled dipole inversion for quantitative susceptibility mapping using structural consistency between the magnitude image and the susceptibility map. *Neuroimage* 2012; 59(3): 2560–2568.

11. Wang Y, Liu T. Quantitative susceptibility mapping (QSM): decoding MRI data for a tissue magnetic biomarker. *Magnetic resonance in medicine* 2015; 73(1): 82–101.

12. Polak D, Chatnuntawech I, Yoon J, et al. Nonlinear dipole inversion (NDI) enables robust quantitative susceptibility mapping (QSM). *NMR in Biomedicine* 2020; 33(12): e4271.

13. Lambert M, Tejos C, Langkammer C, Milovic C. Hybrid data fidelity term approach for quantitative susceptibility mapping. *Magnetic Resonance in Medicine* 2022; 88(2): 962–972.

14. Rasmussen KGB, Kristensen M, Blendal RG, et al. DeepQSM-using deep learning to solve the dipole inversion for MRI susceptibility mapping. *BioRxiv* 2018: 278036.

15. Yoon J, Gong E, Chatnuntawech I, et al. Quantitative susceptibility mapping using deep neural network: QSMnet. *Neuroimage* 2018; 179: 199–206.

16. Jung W, Yoon J, Ji S, et al. Exploring linearity of deep neural network trained QSM: QSMnet+. *Neuroimage* 2020; 211: 116619.

17. Chen Y, Jakary A, Avadiappan S, Hess CP, Lupo JM. QSMGAN: improved quantitative susceptibility mapping using 3D generative adversarial networks with increased receptive field. *NeuroImage* 2020; 207: 116389.

18. Gao Y, Zhu X, Moffat BA, et al. xQSM: quantitative susceptibility mapping with octave convolutional and noise-regularized neural networks. *NMR in Biomedicine* 2021; 34(3): e4461.

19. Gao Y, Cloos M, Liu F, Crozier S, Pike GB, Sun H. Accelerating quantitative susceptibility and R2* mapping using incoherent undersampling and deep neural network reconstruction. *Neuroimage* 2021; 240: 118404.

20. Feng R, Zhao J, Wang H, et al. MoDL-QSM: Model-based deep learning for quantitative susceptibility mapping. *NeuroImage* 2021; 240: 118376.

21. Lai KW, Aggarwal M, Zijl vP, Li X, Sulam J. Learned Proximal Networks for Quantitative Susceptibility Mapping. In: Springer. ; 2020: 125–135.

22. Li Z, Li J, Wang C, et al. Meta-Learning Based Interactively Connected Clique U-Net for Quantitative Susceptibility Mapping. *IEEE Transactions on Computational Imaging* 2021; 7: 1385–1399.

23. Liu J, Koch KM. Meta-QSM: An image-resolution-arbitrary network for QSM reconstruction. *arXiv preprint arXiv:1908.00206* 2019.

24. Oh G, Bae H, Ahn HS, Park SH, Moon WJ, Ye JC. Unsupervised resolution-agnostic quantitative susceptibility mapping using adaptive instance normalization. *Medical Image Analysis* 2022; 79: 102477.

25. Xiong Z, Gao Y, Liu F, Sun H. Affine transformation edited and refined deep neural network for quantitative susceptibility mapping. *NeuroImage* 2023; 267: 119842.

26. Wang Z, Xia P, Huang F, et al. A data-driven deep learning pipeline for quantitative susceptibility mapping (QSM). *Magnetic Resonance Imaging* 2022; 88: 89–100.

27. Gao Y, Xiong Z, Fazlollahi A, et al. Instant tissue field and magnetic susceptibility mapping from MRI raw phase using Laplacian enhanced deep neural networks. *NeuroImage* 2022; 259: 119410.

28. He J, Wang L, Cao Y, Wang R, Zhu Y. Learn Less, Infer More: Learning in the Fourier Domain for Quantitative Susceptibility Mapping. *Frontiers in Neuroscience* 2022; 16.

29. Cognolato F, O'Brien K, Jin J, et al. NeXtQSM—A complete deep learning pipeline for data-consistent Quantitative Susceptibility Mapping trained with hybrid data. *Medical Image Analysis* 2023; 84: 102700.

30. Zhang J, Spincemaille P, Zhang H, et al. LARO: Learned Acquisition and Reconstruction Optimization to accelerate Quantitative Susceptibility Mapping. *NeuroImage* 2023: 119886.

31. Jung W, Bollmann S, Lee J. Overview of quantitative susceptibility mapping using deep learning: Current status, challenges and opportunities. *NMR in Biomedicine* 2022; 35(4): e4292.

32. Zhang J, Liu Z, Zhang S, et al. Fidelity imposed network edit (FINE) for solving ill-posed image reconstruction. *Neuroimage* 2020; 211: 116579.

33. Wang S, Su Z, Ying L, et al. Accelerating magnetic resonance imaging via deep learning. In: IEEE. ; 2016: 514–517.

34. Paszke A, Gross S, Massa F, et al. PyTorch: An Imperative Style, High-Performance Deep Learning Library. *Advances in Neural Information Processing Systems* 2019; 32: 8026–8037.

35. Kingma DP, Ba J. Adam: A method for stochastic optimization. *arXiv preprint arXiv:1412.6980* 2014.

36. Langkammer C, Schweser F, Shmueli K, et al. Quantitative susceptibility mapping: report from the 2016 reconstruction challenge. *Magnetic resonance in medicine* 2018; 79(3): 1661–1673.

37. Mathew RS, Paluru N, Yalavarthy PK. Model resolution-based deconvolution for improved quantitative susceptibility mapping. *NMR in Biomedicine* 2023: e5055. doi: https://doi.org/10.1002/nbm.5055

38. Milovic C, Bilgic B, Zhao B, Acosta-Cabronero J, Tejos C. Fast nonlinear susceptibility inversion with variational regularization. *Magnetic resonance in medicine* 2018; 80(2): 814–821.

39. Wei H, Dibb R, Zhou Y, et al. Streaking artifact reduction for quantitative susceptibility mapping of sources with large dynamic range. *NMR in Biomedicine* 2015; 28(10): 1294–1303.

40. DF-QSM [Code]. https://github.com/NaveenPaluru/DF-QSM; 2023.